Journal of Marine Science and Technology
DOI: 10.6119/JMST-013-0325-1

EFFECTS OF SWEEP ANGLES AND ANGLES OF ATTACK ON JUNCTION-FLOW PATTERNS

Kuo-Ching San[1], Ying-Zong Lin[2], and Shun-Chang Yen[2]

Key words: wing junction, junction vortex, oil flow, sweep angle.

ABSTRACT

This study utilized the NACA 0012 finite wings to investigate the effects of wing sweep angle (Λ) and angle of attack (α) on the junction vortex at $Re = 8 \times 10^4$. The junction-vortex structures were visualized using the surface oil-flow visualization. The junction vortex is classified as — separation, attached, bubble, and bluff-body wake modes. The separation mode occurs at $\Lambda < 12°$ and $\alpha < 5°$. The attached mode occurs at low α for a swept-back wing ($\Lambda > 0°$) and the bluff-body wake mode occurs at high α for a forward-swept wing ($\Lambda < 0°$). Furthermore, the bubble mode occurs at high sweep angle (*i.e*., high backward sweep angle) and high angle of attack. Furthermore, the properties of velocity vectors, normal stress and shear stress are also detected and analyzed using an X-type hot-wire anemometer.

I. INTRODUCTION

For an aircraft, the wing provides the lift to support the aircraft in flight and the fuselage holds the aircrew, passengers or cargos. The wing junction connects the wing and the fuselage. With the constrained three-dimensional wall effect, the boundary-layer separation induces the junction vortex occurring near the wing junction. Namely, the pressure gradient generates three dimensional flow separations near the wing leading edge and wing root. The junction vortex has attracted increasing interest in the aerodynamic and hydraulic issues [6, 8, 9]. In aerodynamic issues, the junction vortex affects the performance of wings, engine turbine, and jet-engine compressors. Furthermore, in the hydraulic issues, the junction vortex scrubs the base of bridge pier, and then damages the bridge.

The experimental study on junction flow was presented by Simpson [9]. Simpson utilized both the bluff and streamlined bodies to investigate the effects of junction vortex on the laminar and turbulent boundary layers. Furthermore, Simpson found that the junction vortex is highly unsteady and has high turbulence intensity, high surface pressure fluctuations except that in the laminar flow occurring at very low Reynolds number. Olcmen and Simpson [6] used the microphones to measure the surface pressure fluctuations for several wing junctions. Furthermore, Olcmen *et al*. applied the surface oil-flow visualization (SOFV) to delineate the streamline patterns on the wing surfaces and probe the pressure-fluctuation near the nose region. They found that the pressure-fluctuation is bimodal. Moreover, the SOFV patterns display the primary separation regions, lines of low shear, and the fish-tail-shaped wake region. Devenport *et al*. [2] investigated the fillet effect to decrease the intensity of horseshoe vortex by changing the angle of attack (α) at 0, 6 and 12 degrees. They indicated that the effects of adding fillet and changing α can not remove the leading-edge separation or the formation of horseshoe vortex. Specifically, the fillet can push the separated flow away from the wing surface. Yen *et al*. [12, 13] changed the angle of attack and Reynolds number (Re) to classify the boundary-layer flow on the swept wings as six characteristic flow patterns. Their results indicated that Reynolds number has weak effect on the distribution of characteristic flow patterns as $Re > 75{,}000$.

Many researchers have focused their interests on the bluff body. Lin *et al*. [5] experimentally visualized the flow structures of horseshoe vortex near the junction of square cylinder and plate using the particle image velocimetry (PIV). They found that the Reynolds number did not influence the flow structures. Furthermore, they classified the horseshoe vortices as — steady horseshoe vortex system; periodic oscillation vortex system with small displacement; periodic breakaway vortex system; and irregular vortex system. Gand *et al*. [3] studied the flow structures near the junction of a wing and a flat fuselage. They found that the horseshoe vortex oscillates with the normalized frequencies of 0.2 – 0.3. Furthermore, Gand *et al*. indicated that the Reynolds number had a dramatic influence on the onset of corner separation. With the analysis of numerical studies, Paik *et al*. [7] utilized the detached-eddy simulation to investigate the formation of dynamical horseshoe vortex. Furthermore, they applied the turbulent boundary layer approach to study the wall-mounted obstacle experiencing a

Paper submitted 10/11/11; revised 03/18/13; accepted 03/25/13. Author for correspondence: Kuo-Ching San (*e-mail: d90543001@ntu.edu.tw*).
[1]Department of Aircraft Engineering, Air Force Institute of Technology, Kaohsiung City, Taiwan, R.O.C.
[2]Department of Mechanical and Mechatronic Engineering, National Taiwan Ocean University, Keelung, Taiwan, R.O.C.

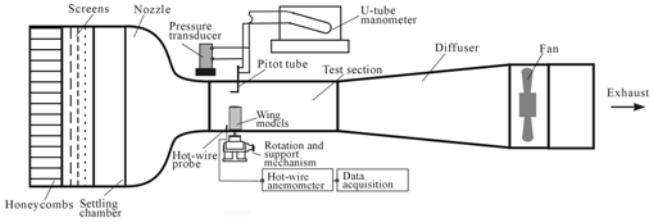

Fig. 1. Experimental setup.

strong adverse pressure gradient and three-dimensional separation. Paik *et al*. determined that the coherent horseshoe vortex occurring in the junction region is caused from the adverse pressure gradient on the wing.

This current investigation studies the formation of junction vortex using various Reynolds numbers, sweep angles, and angles of attack. Furthermore, the decrease of junction-vortex intensity is analyzed and presented. Summarily, the objectives of current investigation is to (1) delineate the flow pattern using the surface oil-flow visualization; (2) classify the flow modes using SOFV patterns; (3) investigate the effect of angle of attack, and sweep angle on the shear stress near the wing junction using the hot-wire anemometry. For future applications, the current results can be utilized in the airfoil performance, gas-engine blade design and civil architecture design.

II. EXPERIMENTS

1. Apparatus

The experiments were tested in an open-channel wind tunnel. A polished aluminum-alloy plate was set as the test-section base, and three highly transparent Polymethylmethacrylate (PMMA) plates were utilized as the roof and lateral plates for flow observation and photography. Figure 1 schematically plots the experimental arrangements. The width, height and length of this wind-tunnel test-section are 50, 50, and 120 cm^3, respectively. Furthermore, the turbulence intensity of free-stream is < 0.4% as the free-stream velocity (u_∞) operated in the range of $0.56 < u_\infty < 45$ m/s. In the wind-tunnel diffuser, an axial fan was utilized to control the free-stream velocity. The free-stream velocity was probed using a Pitot tube connected to an inclined U-tube manometer. The non-uniformity of average velocity across the test section is < 0.5%.

2. Aerofoil

The NACA 0012 [1] airfoils are widely utilized and a large amount of wind-tunnel data is provided. In the current investigation, the aerofoil models were manufactured from stainless steel by milling the sweep angle (Λ) of –45°, –38°, –30°, –15°, 0°, 15°, 30°, 38° and 45°, as shown in Fig. 2. Moreover, the chord length is 6 cm, in which the wing span is 30 cm; and therefore, the aspect ratio is 5. Finally, the airfoil model was mounted on a support, and protruded perpendicularly through the aluminum-alloy base of the test section.

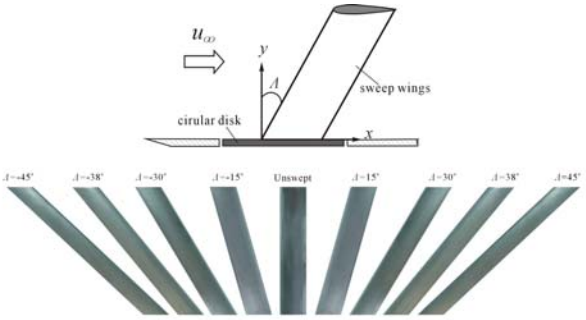

Fig. 2. Configurations of swept wings.

3. Surface Oil-Flow Visualization

Squire theoretically presented the surface oil-flow visualization (SOFV) by painting the wing surface with a visible fluid and then observed the boundary-layer patterns in the fluid [10]. In this investigation, the engine oil mixed with blue dye powder was painted on the wing upper surface. The dark-blue traces on the wing surface delineated the position of accumulated dyed engine oil. The surface-flow direction on wing surface was delineated using the skin-friction lines visualized by the oil flow. The positions of boundary-layer flow separation and reattachment were measured from the video recorder.

4. Hot-Wire Anemometry

The velocity vectors were detected using an X-type hot wire sensor (cross type, TSI 1240-T1.5). The diameter and length of the hot wire were 5 μm and 1.5 mm, respectively, and therefore the dynamic response of hot wire is between 15 and 25 kHz. Finally, the voltage signals of hot-wire anemometer were input the high-speed PC-based data acquisitor.

5. Velocity profile near wing junction

In order to find the wing junction region, Fig. 3 shows the velocity profile and distribution of turbulence intensity (*T.I.*) while the Reynolds number (*Re*) is $Re = 8 \times 10^4$. The origin of *x*-coordinate is located at wing leading edge and the zero point of the *y*-coordinate is set at the wing-root close to the fuselage. The hot-wire anemometer was installed at $x/C = -0.212$ to detect the velocity signal. Furthermore, the test points along the y/C are located from 0.002 to 1.333. Figure 3(a) shows that the distribution of free-stream velocity along the axis of $x/C = -0.212$. In Fig. 3(a), the velocity profile becomes uniform when y/C is >0.208. Namely, the free-stream velocity is not affected by the wall effect when $y/C > 0.208$. Furthermore, Fig. 3(b) shows the distribution of *T.I.* along the axis of $x/C = -0.212$ and $Re = 8 \times 10^4$. The *T.I.* does not change while $y/C > 0.25$.

III. RESULTS AND DISCUSSION

1. Surface Oil-Flow Patterns

Figures 4 and 5 plot the visualized surface oil-flow patterns and sketched flow patterns near the wing junction. In Figs. 4 and 5, the effects of sweep angle, angle of attack on the mode

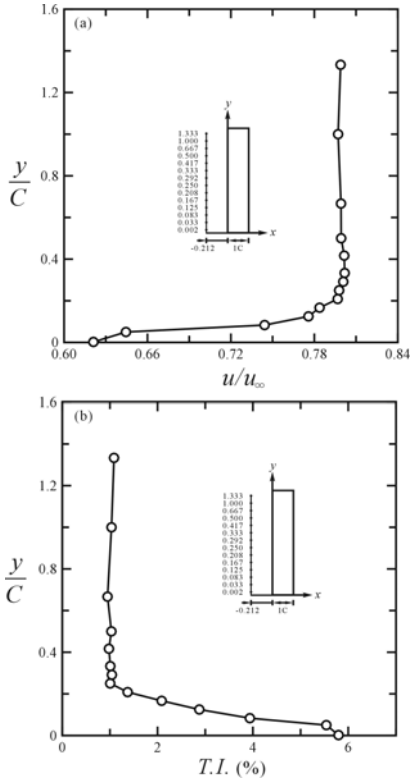

Fig. 3. (a) Distributions of non-dimensional velocity (u/u_∞) with respect to the non-dimensional y coordinate (y/C). (b) Variation of turbulence intensity ($T.I.$) as function of non-dimensional y coordinate (y/C). $Re = 8 \times 10^4$.

distribution are considered at $Re = 8 \times 10^4$. For $\Lambda = -45°$ (*i.e.*, forward swept), Figs. 4(a) and 5(a) display that the separation mode occurs at $\alpha < 5°$, bubble mode occurs at $5° < \alpha < 10°$, and the bluff-body wake mode occurs at $\alpha > 10°$. The bold accumulated blue lines reveal the flow-separation lines. For $\Lambda = -30°$, Figs. 4(b) and 5(b) show that the separation mode occurs at $\alpha < 5°$, bubble mode occurs at $5° < \alpha < 12°$ and the bluff-body wake mode occurs at $\alpha > 12°$. For a straight wing (*i.e.*, unswept and $\Lambda = 0°$), Figs. 4(c) and 5(c) reveal that the separation mode occurs at $\alpha < 5°$, bubble mode occurs at $\alpha > 5°$, Namely, the attached mode does not occurs in the observation range. For $\Lambda = 30°$ (*i.e.*, swept-back wing), Figs. 4(d) and 5(d) demonstrate that the separation mode occurs at $\alpha < 5°$, bubble mode occurs at $\alpha > 5°$ and no attached mode is observed in this investigation range. Furthermore, for a swept-back wing with $\Lambda = 45°$, Figs. 4(e) and 5(e) delineate that the attached mode occurs at $\alpha < 15°$, and the bubble mode occurs at $\alpha > 15°$. Specifically, the separation mode does not exist.

2. Characteristic Flow Patterns

Figure 6 shows the flow-mode distribution with considering the effects of sweep angel and angle of attack for $Re = 8 \times 10^4$. The flow-mode distribution is classified with the flow observation characteristics utilized in Fig. 4. Figure 6 reveals that the separation mode occurs at $\alpha < 5°$ and $\Lambda < 15°$. The attached mode occurs at low α for a swept-back wing ($\Lambda > 0°$) and the bluff-body wake mode occurs at high α for a forward-swept

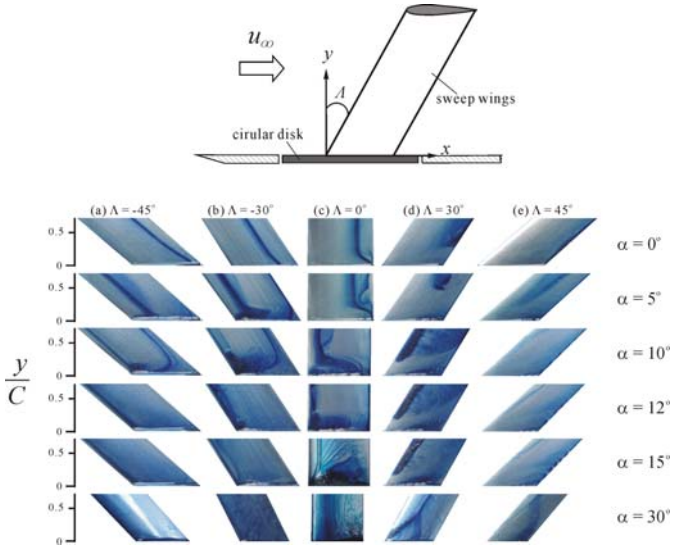

Fig. 4. Surface oil-flow patterns near the wing junction. $Re = 8 \times 10^4$.

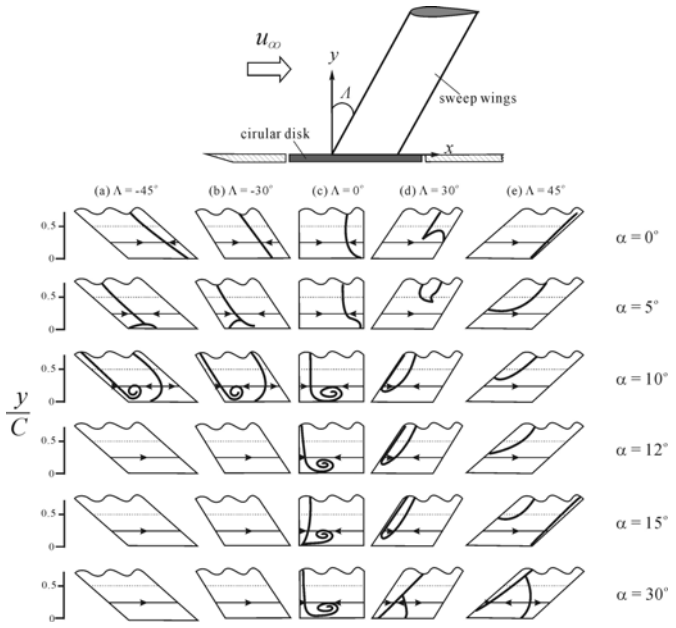

Fig. 5. Sketched surface-flow patterns near the wing junction.

wing ($\Lambda < 0°$). Furthermore, the bubble mode occurs at high sweep angle (*i.e.*, high backward sweep angle) and high angle of attack. The previous studies focus on the prediction of vortex-junction flow patterns at low Reynolds number [4, 6, 9, 11]. These junction-flow patterns at high Reynolds number can be utilized in fuselage scour of high-speed air vehicles.

3. Velocity properties

Figures 7–9 show the velocity-vector characteristics measured using an X-type hot-wire anemometer. For examining the velocity vectors of unsteady junction vortex around the wing root, this X-type hot-wire probe was placed at $y/C = 0.125$.

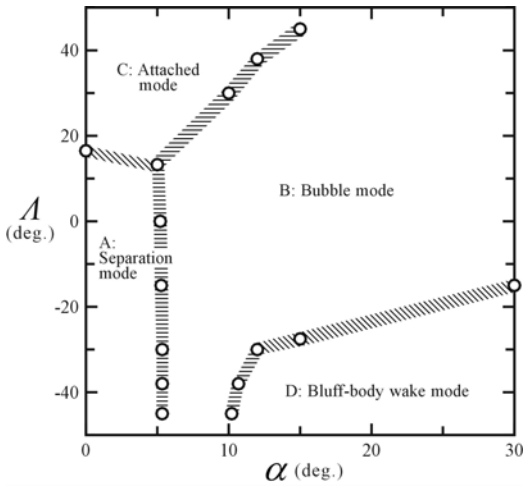

Fig. 6. Distribution of characteristic junction-flow modes. $Re = 8 \times 10^4$.

Furthermore, the velocity components along the x-axis were detected.

Figure 7 reveals the variations of non-dimensional streawise velocity (u/u_∞), transverse velocity (v/u_∞), streamwise normal stress ($\overline{u'u'}/u_\infty^2$), transverse normal stress ($\overline{v'v'}/u_\infty^2$), and shear stress ($\overline{u'v'}/u_\infty^2$) versus the non-dimensional coordinate (x/C) using various angles of attack for a straight wing (*i.e.*, $\Lambda = 0°$). Figures 7(a) and 7(b) show the distributions of u/u_∞ versus x/C ahead and behind the wing junction, respectively. Figure 7(a) displays that u/u_∞ decreases as α increases and u/u_∞ decreases while the airflow moves toward the wing body. Figure 7(b) delineates that u/u_∞ decreases downstream at low α (*i.e.*, $\alpha < 15°$) and u/u_∞ increases for high α ($\alpha > 20°$). Figures 7(c) and 7(d) plot the distributions of v/u_∞ against x/C before and after the wing junction, respectively. In Fig. 7(c), v/u_∞ increases while α increases and the absolute value of v/u_∞ increases as the airflow approaches the wing root. Figure 7(d) shows that the v/u_∞ vector increases for low α and the v/u_∞ vector decreases for high α as the airflow moves downstream. Figures 7(e) and 7(f) depict the variations of $\overline{u'u'}/u_\infty^2$ against x/C near the wing junction. Figure 7(e) reveals that the streamwise normal stress has a significant increase as $\alpha = 90°$ near the wing junction. Furthermore, Fig. 7(f) displays that $\overline{u'u'}/u_\infty^2$ decreases for low α ($\alpha < 15°$) when the airflow moves downstream. However, $\overline{u'u'}/u_\infty^2$ increases for high α ($\alpha > 20°$) while the airflow moves downstream. Additionally, the distributions of transverse normal stress shown in Figs. 7(g) and 7(h) have the similar profiles as the streamwise normal stress shown in Figs. 7(e) and 7(f). Furthermore, Figs. 7(i) and 7(j) depict the variations of shear stress against x/C. The $\overline{u'v'}/u_\infty^2$ increases when the airflow moves toward the wing body. Specifically, $\overline{u'v'}/u_\infty^2$ has a significant jump near the wing root when $\alpha = 90°$. Moreover, Fig. 7(j) shows that the shear stress decreases with the airflow moving downstream for $\alpha < 15°$ and the shear stress increases as the airflow moves downstream when $\alpha > 20°$.

Figure 8 shows the variations of non-dimensional streamwise velocity (u/u_∞), transverse velocity (v/u_∞), streamwise normal stress ($\overline{u'u'}/u_\infty^2$), transverse normal stress ($\overline{v'v'}/u_\infty^2$), and shear stress ($\overline{u'v'}/u_\infty^2$) versus the non-dimensional coordinate (x/C) using various sweep angles at $\alpha = 0°$. Figures 8(a) and 8(b) show the distributions of u/u_∞ versus x/C ahead and behind the wing junction, respectively. Figure 8(a) displays that u/u_∞ decreases while the airflow moves toward the wing body. Figure 8(b) reveals that u/u_∞ approaches toward the specific constants

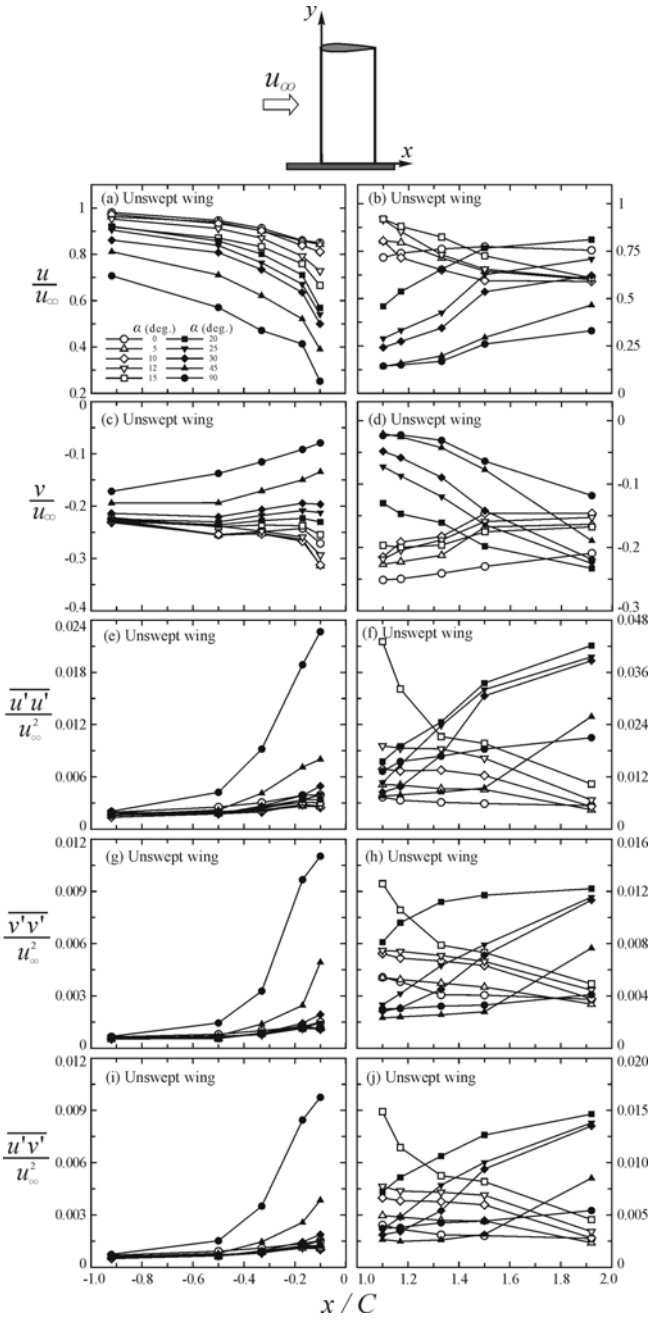

Fig. 7. Variations of non-dimensional streamwise velocity (u/u_∞) transverse velocity (v/u_∞), streamwise normal stress ($\overline{u'u'}/u_\infty^2$), transverse normal stress ($\overline{v'v'}/u_\infty^2$), and shear stress ($\overline{u'v'}/u_\infty^2$) versus the non-dimensional coordinate (x/C) while $\Lambda = 0°$ and $Re = 8 \times 10^4$.

for different sweep angles. Figures 8(c) and 8(d) plot the distributions of v/u_∞ against x/C before and after the wing junction, respectively. In Fig. 8(c), the absolute value of v/u_∞ increases as the airflow approaches the wing root. The velocity vectors of v/u_∞ reveal that the spanwise flow directions of different forward-swept wings are different from those of swept-back wings. Specifically, v/u_∞ has a significant decrease near the wing root as $\Lambda = -45°$. Figure 8(d) shows that the absolute values of v/u_∞ for the swept wings are lower than that of a straight wing. Figures 8(e) and 8(f) depict the variations of $\overline{u'u'}/u_\infty^2$ against x/C near the wing junction. Figure 8(e) reveals that the streamwise normal stresses near the wing root are divided into two groups. The value of $\overline{u'u'}/u_\infty^2$ higher than that of straight wing occurs for the swept-backward wings. Moreover, the value of $\overline{u'u'}/u_\infty^2$ lower than that of straight wing occurs for the forward-swept wings. Furthermore, Fig. 8(f) displays that $\overline{u'u'}/u_\infty^2$ decreases for all the wings when the airflow moves downstream. The distributions of transverse normal stresses, as shown in Figs. 8(g) and 8(h), have the similar profiles as the streamwise normal stresses shown in Figs. 8(e) and 8(f). Furthermore, Figs. 8(i) and 8(j) depict the variations of shear stress against x/C. The $\overline{u'v'}/u_\infty^2$ near the wing root are also separated by the straight wing. The $\overline{u'v'}/u_\infty^2$ higher than that of straight wing occurs for the swept-backward wings, and $\overline{u'v'}/u_\infty^2$ lower than that of straight wing occurs for the forward-swept wings.

Figure 9 shows the variations of non-dimensional streamwise velocity (u/u_∞), transverse velocity (v/u_∞), streamwise normal stress ($\overline{u'u'}/u_\infty^2$), transverse normal stress ($\overline{v'v'}/u_\infty^2$), and shear stress ($\overline{u'u'}/u_\infty^2$) versus the non-dimensional coordinate (x/C) using various sweep angles at $\alpha = 30°$. Figures 9(a) and 9(b) show the distributions of u/u_∞ versus x/C ahead and behind the wing junction, respectively. Figure 9(a) displays that u/u_∞ decreases while the airflow moves toward the wing body. Figure 9(b) reveals that u/u_∞ is approximately constant behind the forward-swept wings. Furthermore, Fig. 9(b) displays that the u/u_∞ increases for $\Lambda < 15°$ and u/u_∞ decreases for $\Lambda > 30°$ while the airflow moves downstream. Figures 9(c) and 9(d) plot the distributions of v/u_∞ against x/C before and after the wing junction, respectively. In Fig. 9(c), the absolute values of v/u_∞ for the swept-back wings increase as the airflow approaches the wing root. However, the absolute values of v/u_∞ for the forward-swept wings decrease when the airflow moves close to the wing root. Figure 9(d) shows that the values of v/u_∞ are approximately constant behind the forward-swept wings. Figures 9(e) and 9(f) depict the variations of $\overline{u'u'}/u_\infty^2$ against x/C near the wing junction. Figure 9(e) reveals that the streamwise normal stresses near the wing root are divided into two groups. For the swept-back wings, $\overline{u'u'}/u_\infty^2$ increases as the airflow moves toward the wing junction. Moreover, the values of $\overline{u'u'}/u_\infty^2$ near the wing root for the forward-swept wings are lower than that of straight wing. Figure 9(f) displays that $\overline{u'u'}/u_\infty^2$ approaches toward different constants for the

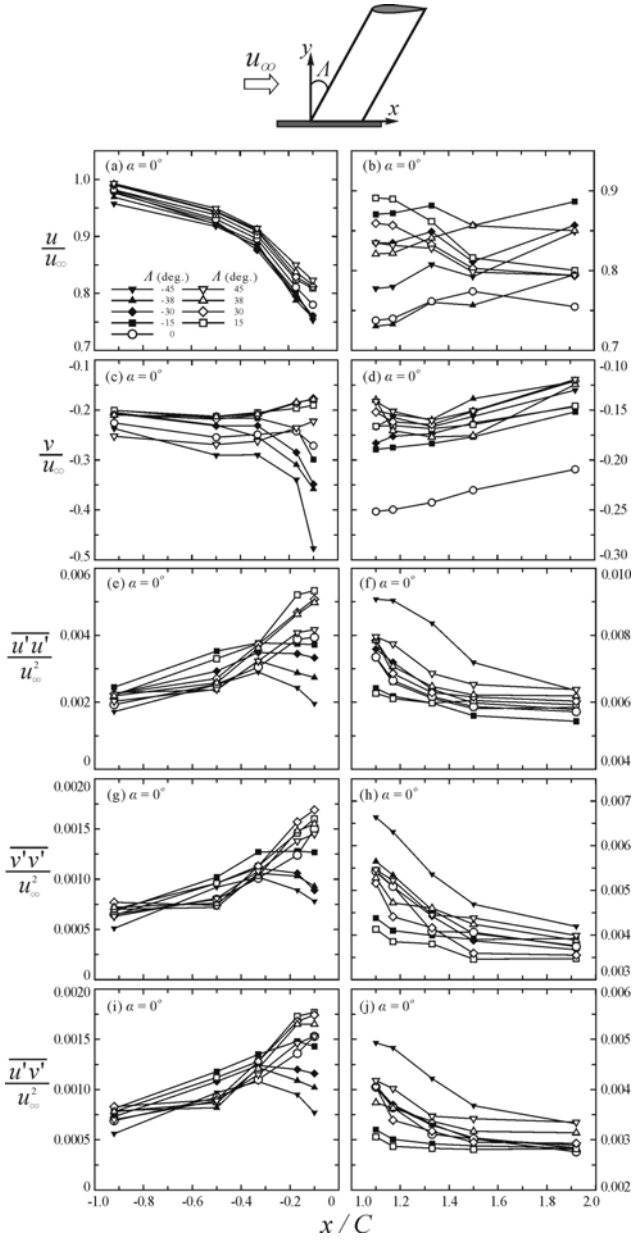

Fig. 8. Variations of non-dimensional streamwise velocity (u/u_∞), transverse velocity (v/u_∞), streamwise normal stress ($\overline{u'u'}/u_\infty^2$), transverse normal stress ($\overline{v'v'}/u_\infty^2$), and shear stress ($\overline{u'v'}/u_\infty^2$) versus the non-dimensional coordinate (x/C) while $\alpha = 0°$ and $Re = 8 \times 10^4$.

swept-back and forward-swept wings, respectively. However, $\overline{u'u'}/u_\infty^2$ behind the straight wing increases while the airflow moves downstream. The distributions of transverse normal stresses shown in Figs. 9(g) and 9(h) have the assemble profiles with the streamwise normal stresses shown in Figs. 9(e) and 9(f). Furthermore, Figs. 9(i) and 9(j) depict the variations of shear stress against x/C. The curves of $\overline{u'v'}/u_\infty^2$ near the wing root are also separated by the straight wing. The value of $\overline{u'v'}/u_\infty^2$ higher than that of straight wing occurs for the swept-backward wings, and $\overline{u'v'}/u_\infty^2$ lower than that of straight

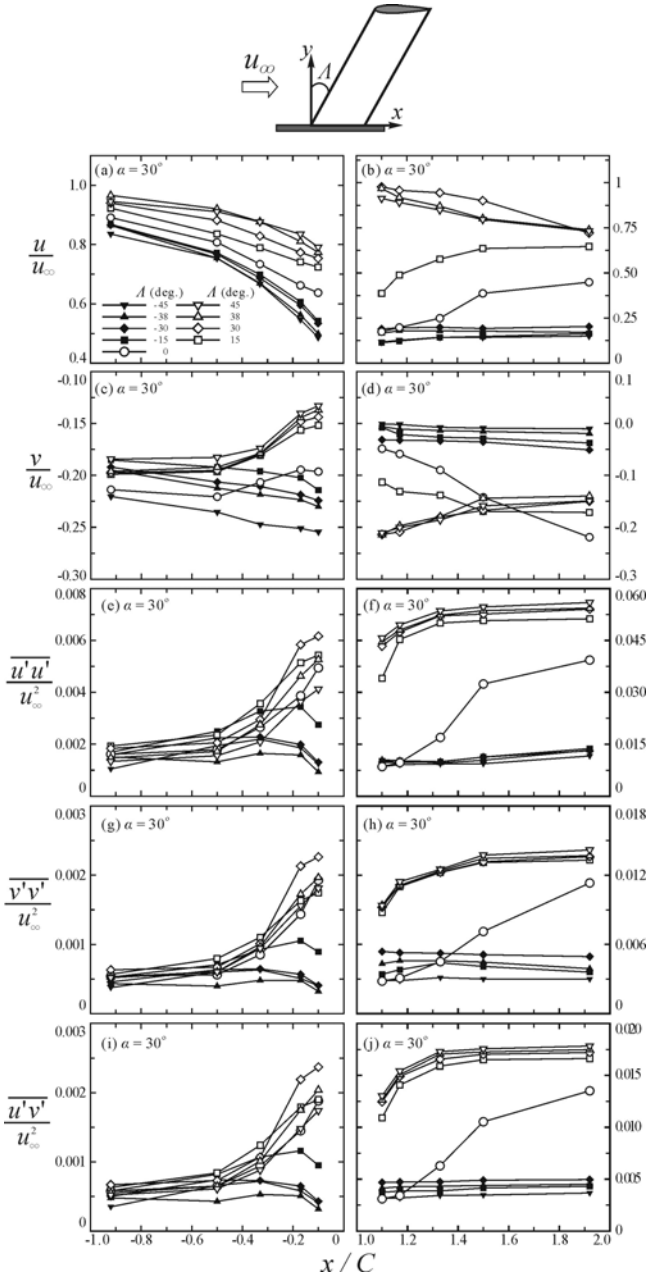

Fig. 9. Variations of non-dimensional streamwise velocity (u/u_∞), transverse velocity (v/u_∞), streamwise normal stress ($\overline{u'u'}/u_\infty^2$), transverse normal stress ($\overline{v'v'}/u_\infty^2$), and shear stress ($\overline{u'v'}/u_\infty^2$) versus the non-dimensional coordinate (x/C) while $\alpha = 30°$ and $Re = 8 \times 10^4$.

wing occurs for the forward-swept wings.

IV. CONCLUSIONS

This study elucidated the characteristics of junction-flow patterns around a NACA 0012 wing with the sweep angle of 0°, –15°, –30°, –38°, –45°, 15°, 30°, 38°, and 45° for $Re = 8 \times 10^4$. Furthermore, the effect of angle of attack on the flow field is also considered. The junction flow is classified as — separation, attached, bubble, and bluff-body wake modes. The separation mode occurs at $\alpha < 5°$ and $\Lambda < 12°$. The attached mode occurs at low α for a swept-back wing ($\Lambda > 0°$) and the bluff-body wake mode occurs at high α for a forward-swept wing ($\Lambda < 0°$). Furthermore, the bubble mode occurs at high sweep angle (*i.e.*, high backward sweep angle) and high angle of attack. For a straight wing (*i.e.*, $\Lambda = 0°$), the non-dimensional streamwise velocity (u/u_∞) decreases as α increases and u/u_∞ decreases while the airflow moves toward the wing body. Furthermore, using the swept wings at $\alpha = 0°$, the streamwise normal stresses ($\overline{u'u'}/u_\infty^2$) near the wing root are divided into two groups. The $\overline{u'u'}/u_\infty^2$ which is higher than that of straight wing occurs for the swept-backward wings and $\overline{u'u'}/u_\infty^2$ lower than that of straight wing occurs for the forward-swept wings. Moreover, for the swept wings fixed at $\alpha = 30°$, the curves of $\overline{u'v'}/u_\infty^2$ near the wing root are also separated by that of straight wing. The value of $\overline{u'v'}/u_\infty^2$ which is higher than that of straight wing occurs for the swept-backward wings, and $\overline{u'v'}/u_\infty^2$ lower than that of straight wing occurs for the forward-swept wings.

V. ACKNOWLEDGMENT

This research was supported by the National Science Council of the Republic of China, under Grant No. NSC 96-2221-E-019-006.

REFERENCES

1. Abbott, I. H. and von Doenhoff, A. E., *Theory of Wing Section*, Dover Publications, New York, pp. 50-53 (1959).
2. Devenport, W. J., Agarwal, N. K., Dewitz, M. B., Simpson, R. L., and Poddary, K., "Effects of a fillet on the flow past a wing-body junction," *AIAA Journal*, Vol. 28, pp. 2017-2024 (1990).
3. Gand, F., Deck, S., Brunet, V., and Sagaut, P., "Flow dynamics past a simplified wing body junction," *Phys. Fluids*, Vol. 22, pp. 115111 (2010).
4. Hwang, J. Y. and Yang, K. S., "Numerical study of vortical structures around a wall-mounted cubic obstacle in channel flow," *Phys. Fluids*, Vol. 16, pp. 2382-2394 (2004).
5. Lin, C., Ho, T. C., and Dey, S., "Characteristics of steady horseshoe vortex system near junction of square cylinder and base plate," *ASCE Journal of Engineering Mechanics*, Vol. 134, pp. 184-197 (2008).
6. Olcmen, S. M. and Simpson, R. L., "Influence of wing shapes on surface pressure fluctuations at wing-body junctions," *AIAA Journal*, Vol. 32, pp. 6-15 (1994).
7. Paik, J., Escauriaza, C., and Sotiropoulos, F., "On the bimodal dynamics of the turbulent horseshoe vortex system in a wing-body junction," *Phys. Fluids*, Vol. 19, pp. 045107 (2007).
8. Shekarriz, A., Fu, T. C., Katz, J., Liu, H. L., and Huang, T. T., "Study of junction and tip vortices using particle dispacement velocimetry," *AIAA Journal*, Vol. 30, pp. 145-152 (1992).
9. Simpson, R. L., "Junction flows," *Annual Review of Fluid Mechanics*, Vol. 33, pp. 415-443 (2001).
10. Squire, L. C., "The motion of a thin oil sheet under the steady boundary layer on a body," *Journal of Fluid Mechanics*, Vol. 11, pp. 161-179 (1961).
11. Thompson, M. C. and Hourigan, K., "Prediction of vortex junction flow upstream of a surface mounted obstacle," *Proceedings of the 11th Australasian Fluid Mechanics Conference*, Hobart, Australia, pp. 111-114 (1992).
12. Yen, S. C. and Hsu, C. M., "Influence of boundary layer behavior on aerodynamic coefficients of a swept-back wing," *ASME Journal of Fluids Engineering*, Vol. 129, pp. 674-681 (2007).
13. Yen, S. C. and Huang, L. C., "Flow patterns and aerodynamic performance of unswept and swept-back wings," *ASME Journal of Fluids Engineering*, Vol. 131, pp. 111101 (2009).